Pergamon

Int. J. Solids Structures Vol. 32, No. 15, pp. 2191–2218, 1995

0020-7683/95 $9.50 + .00

0020-7683(94)00249-5

INVESTIGATIONS OF HIGH TEMPERATURE DEFORMATION AND CRACK GROWTH UNDER VARIABLE LOAD HISTORIES

F. W. BRUST
Battelle, 505 King Avenue, Columbus, Ohio 43201-2693, U.S.A.

(*Received* 29 *October* 1993; *in revised form* 24 *September* 1994)

Abstract—Time dependent deformation and crack growth behavior under variable load conditions are investigated in this study. Experimental observations of load/unload effects in cracked creeping bodies are first discussed. Then a detailed analysis of a typical test result is presented. The potential of integral parameters, including the T^*-integral, to characterize this complex response, is shown.

1. INTRODUCTION

The demands for structural systems to perform reliably under severe operating conditions continue to increase. Time dependent deformation and corresponding damage development can be the limiting design feature for engineering structures that operate at high temperatures. This is true for both monolithic and composite materials. Time dependent degradation may also be a contributing factor to reducing life even at room temperatures and below [see, for instance, Brust and Leis (1992)].

Most of the studies of time dependent or creep crack growth have been concerned with simplified load conditions and constitutive relations. The methods developed by Riedel (1987) and extended into useful and practical engineering methods by Saxena (1991) are all based on simplified constitutive relations. Indeed, creep fracture parameters such as C^*, C_h^* (Riedel, 1987), C_t (Saxena, 1991), Q^* (Yokobori, 1984), $C(t)$ (Bassani, 1981), and others, are based on the assumptions of strain hardening primary creep law and/or Norton creep. Moreover, simple creep-fatigue engineering approaches rely on Miner's Rule, where the effects of creep crack growth and fatigue are considered separately for predictive purposes, as typified by Jaske's (1984) approach.

The approaches described above can provide useful engineering predictions of creep crack growth, especially under constant load conditions. However, for structural components that operate in a severe thermal environment, including thermal load-history effects in the analysis procedure is essential for accurate crack growth predictions. Indeed, the series of papers recently produced out of the AFWAL Materials Laboratory at Wright–Patterson Air Force Base [see Nicholas and Weerasooriya (1985, 1986) and the references therein] have clearly identified the importance of load history on crack growth behavior. This work, mainly applied to crack growth in the turbine disks of advanced military gas turbine engines made of IN100, consisted of a series of experiments and corresponding numerical analyses of this problem. The numerical analyses included more appropriate constitutive relations than the simple power law type theories discussed above. Useful design models to enable the Retirement for Cause philosophy to be used were developed for handling the creep/fatigue interactions for the turbine disk problem.

Kim *et al.* (1988, 1992) have been studying creep crack growth behavior under severe operating conditions as part of the NASA Hot Section Technology program. They have found that near field integral parameters have the ability to characterize creep crack growth under complex thermal mechanical loading conditions. The other simplified parameters discussed above could not characterize the behavior.

With the above comments in mind, this paper presents an investigation of the fundamental processes that develop in cracked bodies which experience history dependent loading. The paper begins by discussing some general considerations regarding cyclic creep

and experimental observations of this process. A detailed analysis of one of the experiments is then described. As part of this discussion, the importance of proper constitutive laws on response, discussion of asymptotic approaches, and the ability of integral parameters to characterize the response is provided.

2. GENERAL CONSIDERATIONS

The phemonema of creep response under *stress reversals* may be explained as follows. If a uniaxial (metal) bar is heated to a temperature in the materials creep range and then loaded, the following response may be observed [see Gittus (1975) or Murakami and Ohno (1982) for instance]. As creep deformations advance, dislocations lose their mobility as they pile up at obstacles or owing to the formation of various networks, i.e. hardening is induced. These dislocations consist of two parts:

(i) a reversible part, which recovers mobility upon stress reversals; and
(ii) an irreversible part, which has formed irreversible networks.

When the stress in the bar is reversed from tension to compression, or from compression to tension, the reversible dislocations of type (i) remobilize in a direction directly opposite to those previously immobilized. This induces a significant creep strain rate, which may be attributed to material softening. With time, after the stress reversal, the (i) dislocations again become immobilized, and they again start to form irreversible dislocation networks.

If a structural component, or a portion of a component experiences stress reversals, significant creep strain rates are reintroduced. These strain rates cannot be neglected. Moreover, classical creep constitutive laws such as Norton's law or strain hardening laws do not account for this effect.

When a cracked component is loaded in the creep regime, creep strains accumulate from the crack tip outward. When the component is unloaded globally to zero load or even a net positive load, a region of compressive stresses *always* develops near the crack tip. That is, the tensile stresses in the crack tip region at the end of the load-hold period reverse sign upon unloading. This happens because of elastic stress recovery that occurs in the crack tip region where a localized creep zone has developed during the load-hold period. These compressive stresses cause large compressive creep strain rates in the crack tip region. Upon reloading, these compressive stresses that develop during the unload-hold period again reverse sign to tension. This again induces large tensile creep strains, which emanate outward from the crack tip region.

Thus, it is seen that cyclic loading in the creep regime in cracked bodies causes significant creep strain rate reversals, and corresponding increased crack tip strain development. The size of the zone of stress reversals depends on several factors, including load magnitude and amount of creep strain. Under severe conditions (which are increasingly being demanded of structural components), this effect is very important.

The next section describes some of the consequences of this stress reversal effect on the creep crack growth process. This is done by observing the response of creep crack growth specimens that are subjected to variable loads. The analysis sections will also show vivid examples of the above-described processes.

3. EXPERIMENTS OF VARIABLE LOAD CREEP

Before reporting the experimental observations, a description of the experimental procedure is provided.

3.1. *Experimental procedure*

All specimens are standard 1T compact tension specimens with a nominal thickness of 25.4 mm and width (W) of 50.8 mm, which were machined and fatigue precracked prior to testing. The specimens had approximately 20% side grooves machined into them to enforce straight crack growth. During the initial testing phase, one specimen experienced

failure of one of the electric potential (EP) leads that measure crack growth rates, which led to incomplete crack growth data. Two separate EP leads were then used for all other tests.

For the variable load tests, the experimental technique is automated, with the load history programmed on an Instron Servohydraulic machine. This required development of a novel spring-loaded extensometer system. Data acquisition was triggered by load changes. This resulted in rapid data acquisition after load changes, and slower data acquisition during the load-hold periods, which is desired for testing the analysis results. Figure 1 provides a view of the test set-up.

3.2. *Experimental observations regarding variable load creep*

Experimental results on three 9 Cr–Mo tests that were subjected to three different load/unload sequences are described here. Tests have also been performed on 316 stainless steel at two different temperatures, with results indicating the same trends as are to be reported here. [Some of these results may be found in Brust *et al.* (1993) and Brust and Majumdar (1994), and other results will be reported soon.]

Let us first examine some of the general conclusions that can be made regarding history dependent loading in the time dependent deformation regime. Figure 2 illustrates a load versus time sequence that was applied to one of the 9 Cr–Mo compact tension specimens at 538°C. All were fatigue precracked prior to testing. As seen in Fig. 2a, an initial load period of 36 h was made to ensure the development of an initial creep zone in the specimen. The unload-hold times and subsequent reload times were continually decreased until about 90 h, after which 4-h hold periods and 1-h unload periods were maintained until the specimen failed. This assured a truly variable load history.

An enlargement of the displacement versus time history for this experiment between 325 and 365 h, after beginning the test, is illustrated in Fig. 2b. This specimen failed after about 400 h. Another specimen was loaded to the same load level and was identical in all other ways to the above-described specimen except for a slightly larger initial crack. However, this specimen was held for 320 h before unload/reload occurred, and only one cycle was applied. Figure 3 illustrates the displacement versus time history for this test. Note that this test failed at more than 600 h.

Several important general conclusions can be drawn from these results, as follows.

- During the unload-hold period, load-point displacement recovery occurs (Fig. 2b). This is due to the compressive stresses that develop at the crack tip during unload. This zone of compressive stresses near the crack tip can be quite large, as was verified through computational studies, even though the global load is never less than zero. The compressive stress zones will be illustrated later.
- After reload, the displacement rates increase as compared with the rates during the previous loading period. This is clearly seen in Figs 2b and 3. Note also that the displacement just after reloading is always smaller than the corresponding value just before unloading.
- Load history effects significantly decrease life as compared with the nearly constant load (only one unload) test, i.e. in this case the constant load test lasted nearly 1.5 times as long.

Further evidence of this behavior can be seen by observing the results of another test on 9 Cr–Mo steel, also at 538°C. However, the applied load was smaller than in the above tests, and the load sequence is as illustrated in Fig. 4a. As seen, the unload-hold times were only 5 min (as compared with the minimum hold time of 1 h in Fig. 2a). Figure 4b illustrates the load-point displacement response of this specimen before crack growth began. This was a long test, taking over 30 days, and crack growth began at about 192 h after the test began. Figure 4b shows that, as with Figs 2b and 3, the load-point displacement rates (i.e. slope of the curve) increase after an unload compared with the rates before unloading, even before crack growth begins. However, as seen in Fig. 4c, the change in displacements after

an unload/load sequence becomes greater as time proceeds. This particular test has been completely analyzed, and the results will be presented later.

4. ANALYSIS RESULTS

This section will provide several types of analysis results that illustrate the effect of load history on time dependent crack growth and fracture. The first topic discussed involved observations of asymptotic fields that develop under cyclic creep. This is interesting, since most work to date and most practical approaches to the creep crack problem are based on asymptotic solutions using very simple constitutive relations. Here we compare some asymptotic solutions using several types of constitutive laws, including classical and more advanced creep models, which are capable of adequately predicting cyclic response under creep conditions. The second topic briefly examines some integral parameters that are being examined regarding their ability to characterize variable load creep crack growth. The final analysis topic presents the results of the third creep crack problem illustrated in Fig. 4. This test was analyzed throughout the entire 700 h test by using an appropriate constitutive law. The performance of the integral parameters, as well as comparisons with experimental data, is illustrated. Before this, a brief discussion of the computational tools used to develop these solutions is provided.

4.1. *Constitutive laws and finite element code*

The creep behavior of metals under a constant sustained load is classified into three phases: primary, secondary, and tertiary creep. In this work, which considers creep crack growth under variable loads, tertiary creep is not considered, since it occurs only in a small process region near the tip. The influence of the constitutive model used to represent time dependent materials on the stress and strain fields in the vicinity of a crack tip has been shown to be significant (Leung *et al.*, 1988), *even for constant sustained load.* As discussed in Section 2, upon stress reversal, a temporary increase in strain rate has been observed that was due to strain softening. Classical time or strain hardening (S-H) creep laws, upon which most of the current engineering approaches to predicting creep crack growth are based, are incapable of predicting these phenomena. The next section will clearly illustrate this. In the Inoue benchmark problems (Inoue *et al.*, 1991), a model developed by Murakami and Ohno (1982) and improved by Ohno *et al.* (1985) provided as good or better predictions of a complex load response in the creep regime than more than ten different models. The Murakami–Ohno (M–O) law has the advantage of having very simple material property requirements. The mathematical structure and the complicated effort required to obtain material properties for other recently proposed constitutive models render their use in numerical analyses of the creeping crack problem cumbersome.

The constitutive law used for most of the creep crack growth analyses presented here is based on the concept of a creep hardening surface (CHS) developed by Murakami and Ohno (1982, 1985). This model is quite convenient since the material property requirements consist of only the classical time hardening material constants (A, n, m), and the two Norton law constants $[A_1, n_1$; see eqn (1)].

For the general multi-axial case, the creep strain rate in this model is given by:

$$\dot{\varepsilon}_{ij}^{c} = C(\bar{\sigma}, q)S_{ij} = \tfrac{3}{2}m(A)^{1/m}(\bar{\sigma})^{(n-m)/m}(q)^{(m-1)/m}S_{ij} + \tfrac{3}{2}A_1(\bar{\sigma})^{n_1-1}S_{ij}, \tag{1}$$

where S_{ij} and σ are the deviatoric and equivalent stress, respectively. In eqn (1), q is given by:

$$q = \rho + \left(\frac{\varepsilon_{ij}^{c} - \alpha_{ij}}{\bar{\sigma}}\right)S_{ij}. \tag{2}$$

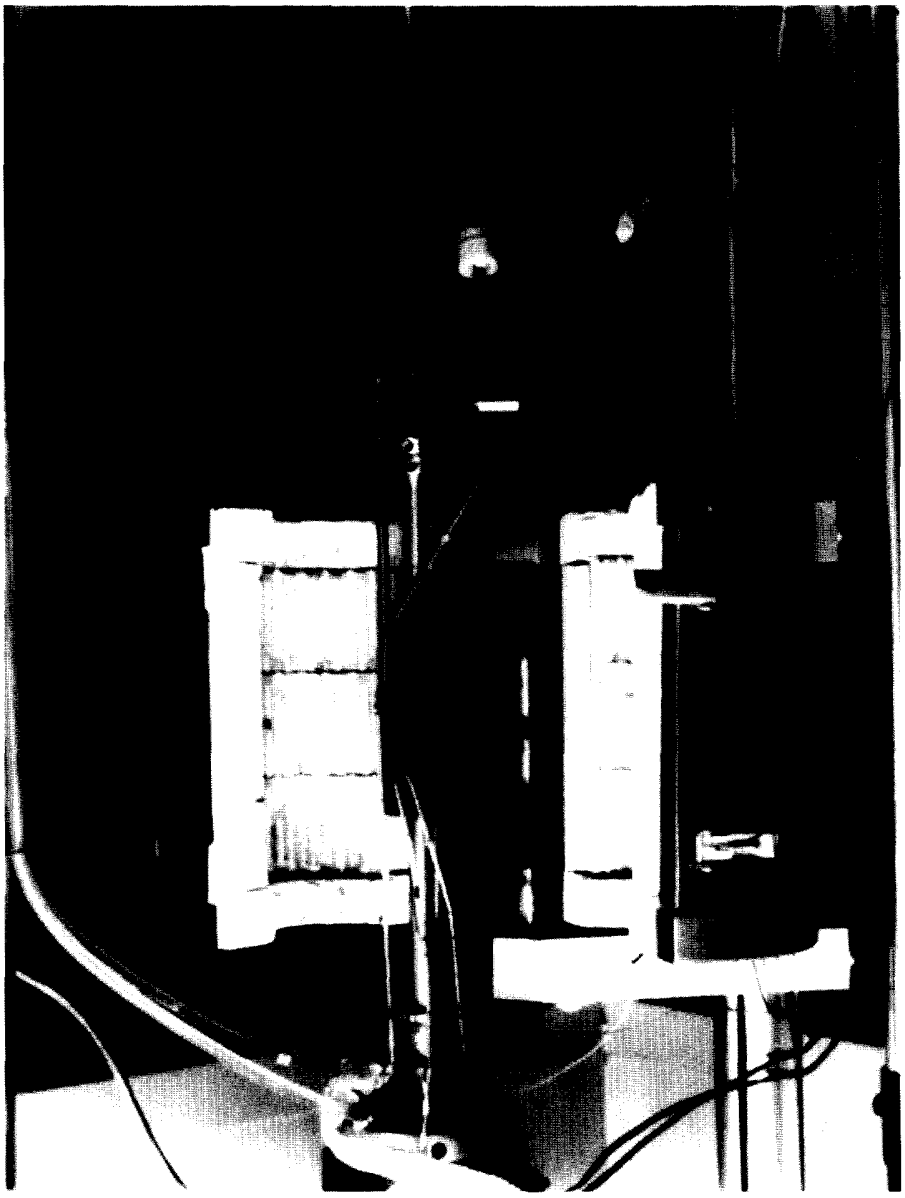

Fig. 1. Photograph of experimental set-up. An instrumented compact tension-specimen is shown here. The load pins go through the specimen. Note the spring-loaded extensometer entering the furnace from the top. This was used to measure crack opening displacements.

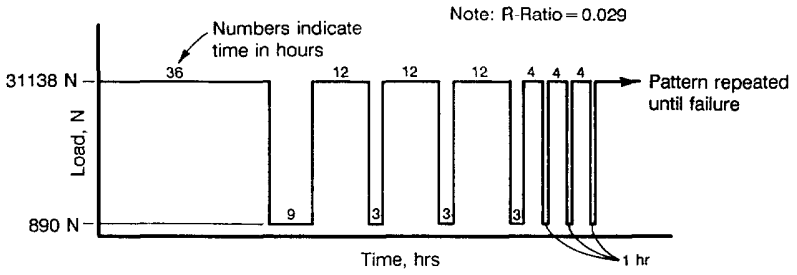

Fig. 2a. Load–time sequence applied to the first 9 Cr–Mo test. The initial crack size (a_0) was 26.75 mm, and $a_0/W = 0.527$.

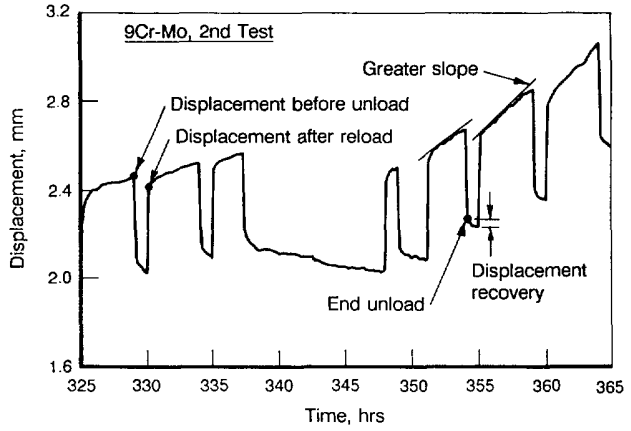

Fig. 2b. Displacement–time history for first 9 Cr–Mo test between 325 and 365 h.

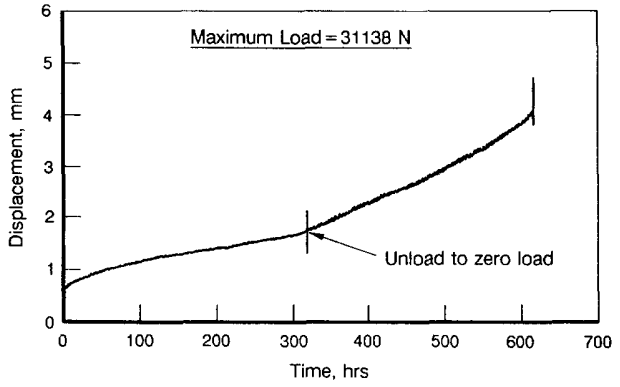

Fig. 3. Displacement–time history for second 9 Cr–Mo test. The load magnitude was identical to the load of Fig. 2a, but only one unload at time of about 320 h occurred. The initial crack size, a_0, was 27.23 mm with $a_0/W = 0.536$.

The evolution equations for the center of the yield surface α_{ij} and radius ρ are given by:

$$\dot{\alpha}_{ij} = \dot{\rho} = 0 \quad \text{if} \quad g < 0 \quad \text{or} \quad \frac{\partial g}{\partial \varepsilon^c_{ij}} \dot{\varepsilon}^c_{ij} \leqslant 0 \tag{3}$$

with

$$\dot{\alpha}_{ij} = \tfrac{1}{2}(\dot{\varepsilon}^c_{kl}\eta_{kl})\eta_{ij}; \quad \dot{\rho} = \frac{1}{\sqrt{6}} \dot{\varepsilon}^c_{ij}\eta_{ij} \quad \text{if} \quad g = 0 \quad \text{and} \quad \frac{\partial g}{\partial \varepsilon^c_{ij}} \dot{\varepsilon}^c_{ij} > 0, \tag{4}$$

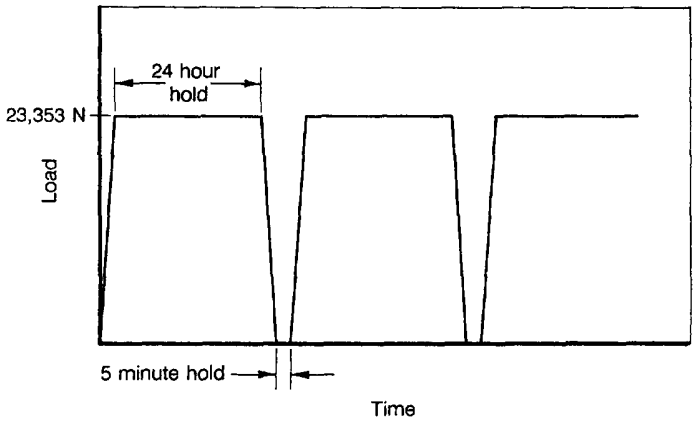

Fig. 4a. Load–time sequence for the third 9 Cr–Mo test.

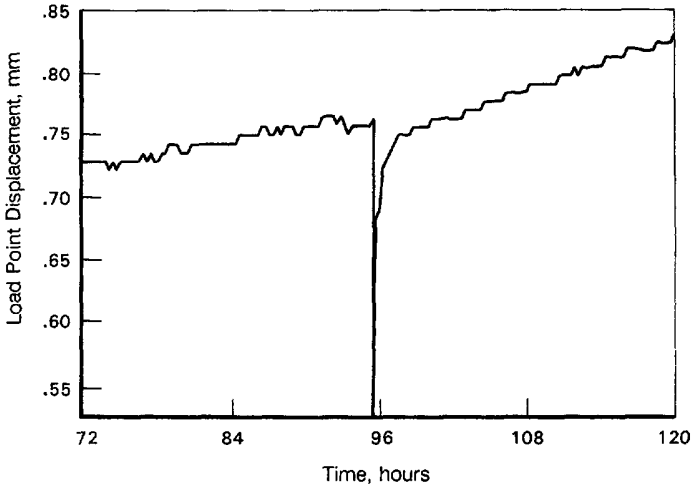

Fig. 4b. Load-point displacement versus time behavior between 72 and 120 h. Note in this specimen crack growth began at about 192 h (a_0 = 23.75 mm).

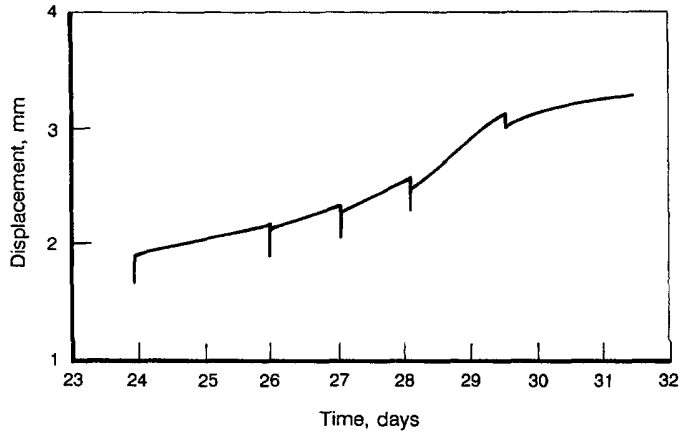

Fig. 4c. Displacement–time record for third test between the 24th and 30th days.

where η_{ij} is the outward normal vector to the CHS defined as

$$\eta_{ij} = \frac{\varepsilon^c_{ij} - \alpha_{ij}}{\{(\varepsilon^c_{kl} - \alpha_{kl})(\varepsilon^c_{kl} - \alpha_{kl})\}^{1/2}}. \tag{5}$$

The CHS is given as

$$g = \tfrac{2}{3}(\varepsilon^c_{ij} - \alpha_{ij})(\varepsilon^c_{ij} - \alpha_{ij}) - \rho^2 = 0 \text{ on CHS} \tag{6}$$

and

$$< 0 \text{ inside.}$$

The radius and center of the CHS therefore change only when the material state is on the CHS ($g = 0$) and remain the same when the state of creep strain is inside the CHS ($g < 0$).

From the evolution equations, it can be easily shown that q becomes $\bar{\varepsilon}_c$ (the equivalent creep strain) when stress reversals do not occur. Thus a principal advantage of this theory is that it coincides with classical creep constitutive laws when they apply. All material constants are therefore easily obtained from uniaxial creep data, which exist for most materials.

When a stress reversal occurs, q of eqn (2) becomes small, which renders the creep strain rates predicted in eqn (1) large. This accounts for large increases in creep strain rates observed experimentally during stress reversals [see Murakami and Ohno (1982, 1985) and Krishnaswamy *et al.* (1994)]. Classical laws upon which most creep fracture theories are based cannot account for this effect. Plasticity is included in this model by assuming that these strains occur over a very short time in evaluating the creep material constants.

A finite element (FE) algorithm using an implicit scheme has been developed for the Ohno and Murakami constitutive model and discussed by Krishnaswamy *et al.* (1993, 1994). The implicit method used here has the advantage of ensuring a convergent and stable solution for large time step sizes, unlike explicit integration schemes. The details of the algorithm have been omitted here and may be found in the cited references. Numerous comparisons using the implicit algorithm are compared with experimental data and with strain hardening theory and are also presented by Krishnaswamy *et al.* (1994) with good results.

The computational model for all analyses consisted of eight-noded isoparametric elements using plane stress or plane strain assumptions. Crack growth was modeled by using a node release technique whereby the nodal forces at both nodes in the particular element through which the crack is growing are released simultaneously over a period of time. The integral fracture parameters were calculated by using existing element shape functions and nodal averaged field quantities using a direct approach (i.e. a domain integral approach, which is convenient for three-dimensional problems, was *not* used). The analysis of the third experiment (Fig. 4) required a great deal of effort on a Cray computer system.

4.2. *Asymptotic observations*

Most practical methods for predicting the lives of cracked structural components that operate at temperatures at which creep occurs are based on a series of asymptotic solutions. These solutions were developed by using simple constitutive laws and are, for the most part, strictly valid for monotonic load-hold conditions [see Goldman and Hutchinson (1975), Riedel (1981), Riedel and Rice (1980), and the summaries provided by Riedel (1987)]. [Note that Riedel (1987) does provide an asymptotic solution for cyclic loading by using Norton's creep law, but the usefulness of this solution is unclear since Norton creep is inaccurate under cyclic load conditions.] Saxena and Han (1986) and Saxena (1991) (and many references cited therein) then developed engineering methods based on parameters that characterize the strength of these fields. In the following examples, we illustrate that the structures of these near tip fields change with time and load cycles, precluding the use of a single asymptotic strength parameter for cyclic load applications.

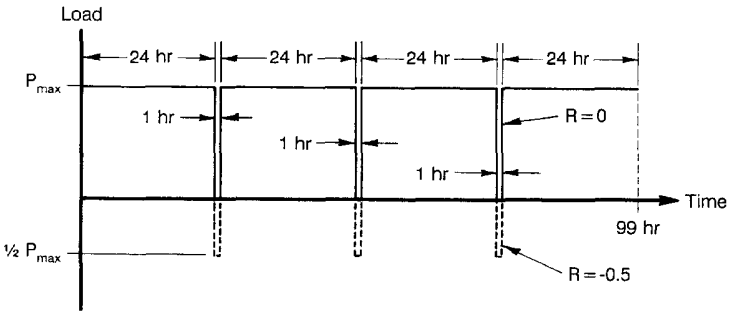

Fig. 5. Load spectra applied to asymptotic problem. Both $R = 0$ and $R = -0.5$ were considered. $P_{max} = 10$ kN for the 304 SS analysis, and $P_{max} = 23.353$ for the 9 Cr–Mo analysis.

Asymptotic solutions. The stress and strain fields near a crack tip are evaluated by using both the classical strain hardening creep law and the Murakami–Ohno (M–O) law [eqn (1)], the former of which is a special case of the M–O law. Cyclic loads are considered and the solutions are developed numerically by using the above-described finite element methodology. Only the first terms in eqn (1) are used since the primary creep term dominates during load changes.

Consider a standard compact tension specimen with crack length $a = 23.75$ mm and uncracked ligament length $c = 27.05$ mm. A finite element analysis of this specimen was performed by using creep properties of both 9 Cr–Mo Steel at 538°C and 304 stainless steel (SS) at 650°C. The applied load spectrum is shown in Fig. 5. Note from Fig. 5 that an $R = 0$ and an $R = -0.5$ spectrum were both used. This spectrum was applied up to 99 total hours. This means that the ends of the load-hold periods were 24, 49, 74, and 99 h while the *ends* of the unload-hold periods were 25, 50, and 75 h (four load and three unload periods). The material properties are:

$$A = 7.09 \times 10^{-17}, \quad n = 5.6, \quad m = 0.24 \quad (9\,\text{Cr–Mo})$$

$$A = 3.10 \times 10^{-19}, \quad n = 7.2, \quad m = 0.54 \quad (304\,\text{SS})$$

for stress in MPa and time in hours. These same constants are used for a strain hardening law and for the Murakami–Ohno cyclic creep law.

The symmetric finite element mesh was a focused mesh with ten rings of six-noded isoparametric triangular elements surrounding the crack tip and eight-noded elements elsewhere. The element size at the crack tip is about 0.00048 c, which is about two-and-one-half times more refined than the mesh used by Shih and German (1981) in their studies of HRR field dominance.

Figure 6(a) provides a plot of the shear creep strain rates just after two of the unload periods for the 304 SS with the $R = 0$ spectrum. This is a plot of $\dot{\varepsilon}_{r\theta}$ as a function of angle, θ, at a constant radius of 0.086 mm from the crack tip (standard crack tip polar co-ordinate definitions are used, with $\theta = 0$ ahead of the crack tip, and $\theta = \pi$ along the crack faces). This distance corresponds to about the seventh ring of elements away from the crack tip. Immediately afterwards the unloads occur at the first unload (time = 24+h) and third unload (time = 74+h), large stresses develop, which emanate from the crack tip. These stresses are relaxed with rather large creep strain rates. From Fig. 6(a), the maximum shear strain rates occur at an angle of about $\pi/2$, and it is clear that using a classical strain hardening creep law greatly underpredicts these strain rates. Figure 6(b) shows the shear creep strain rates at the end of the 1-h unload-hold period. Note that the position of maximum strain rate has shifted to about 1 radian. The strain rates have relaxed significantly; however, the rates from the Murakami–Ohno law are still higher than those of the classical law. All other components of creep strain rate exhibit a similar behavior at this location, and at all other locations.

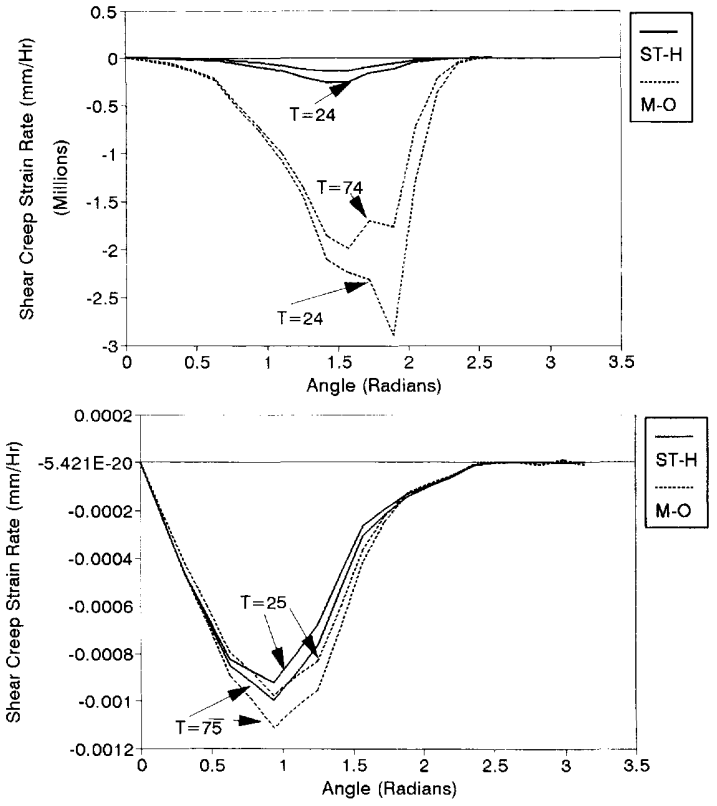

Fig. 6. Shear creep strain rates ($\dot{\varepsilon}^{c}_{r\theta}$) at a constant value of radius, 0.086 mm from the crack tip. (a) Just after the first and third unloads (t = 24, 74 h). (b) At the end of the hold times (t = 25, 75 h).

Figures 7(a)–7(c) show the θ component of stress at an angle of zero, also as a function of distance ahead of the crack tip. Figures 7(a)–7(c) show the stresses at the end of the hold times for 304 SS; $R = 0$, 304 SS; $R = -0.5$, and 9 Cr–Mo; $R = 0$ cases, respectively. Note that these plots show stresses versus $\log(r)$. The solutions for the Murakami–Ohno case, which has much better capability for modeling stress reversals, appear linear on these plots. Although certainly not proven here, it appears that the asymptotic fields behave as:

$$\sigma = C_1 \log(C_2 r). \tag{7}$$

In fact, this apparent logarithmic singularity appears to dominate over a very large distance, and, at least for these cases, does not change with cycle. On the other hand, the stress field when a strain hardening law is used appears to vary as a function of cycle number. Note also that the differences between the S–H and M–O solutions increase as the cycle number increases.

Figures 8a and 8b show the accumulated strains (ε_θ at $\theta = 0$) for the 9 Cr–Mo case, at the end of the unload-hold periods (times 25, 50, 75 h), and at the end of the load-hold periods (times 24, 49, 74 h), respectively. The differences between the S–H and M–O solutions increase as the number of cycles proceeds. Moreover, the strains at the end of the load-hold times are close, independent of the number of cycles for the S–H model. Note that these are the total accumulated creep strains, obtained by integrating the creep strain rates throughout the load history, as appropriate. An interesting observation can be made regarding the results of Figs 6–8. The stresses tend to be higher when a strain hardening law is used than when the Murakami–Ohno law is used, whereas the creep strains are lower. This can be explained as follows. During the load changes, the creep strain rates are greatly under-predicted by using a strain hardening law, whereas they are adequately predicted by using the Murakami–Ohno law. Because of this, the stresses do not relax after load path

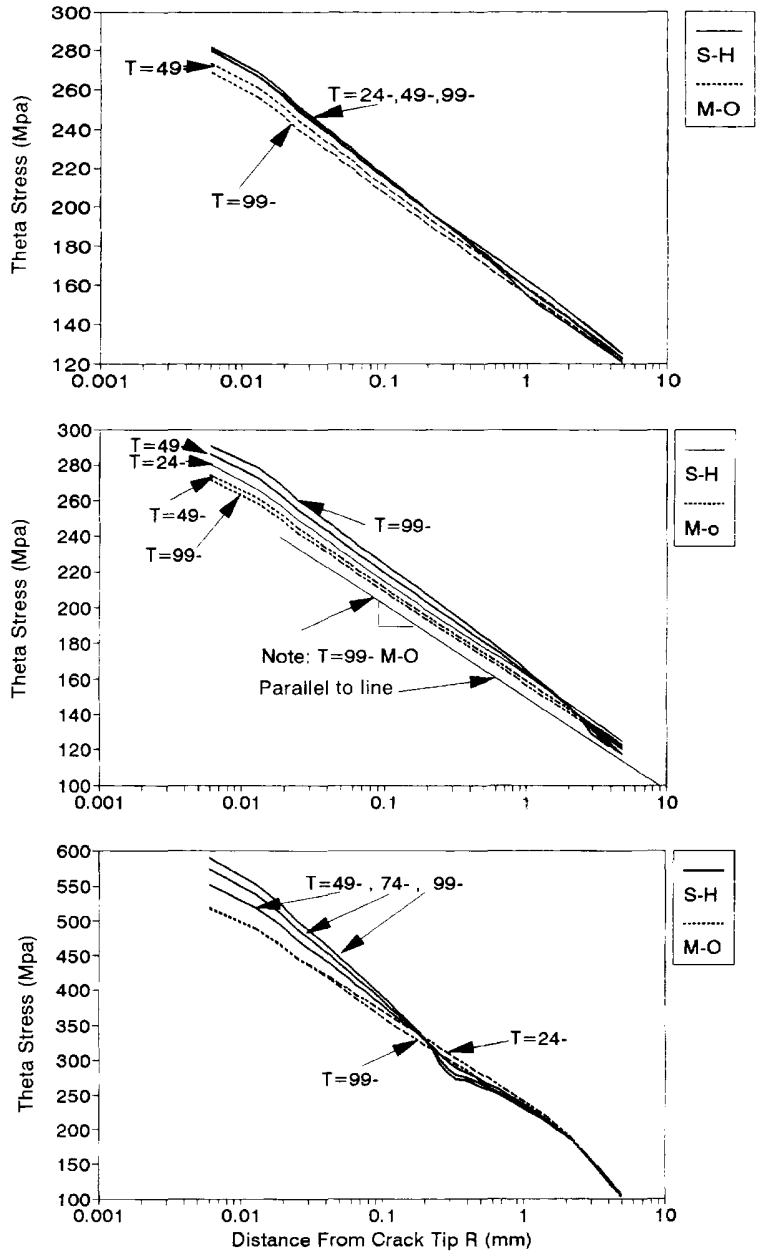

Fig. 7. σ_{θ} Stresses plotted as a function of distance from the crack tip for $\theta = 0$. Results are for times of 24, 49, and 99 h, i.e. after reload-hold sequences. (a) 304SS, $R = 0$ case. (b) 304SS, $R = -0.5$ case. (c) 9 Cr Mo, $R = 0$ case.

changes as much as they should when a strain hardening law is used. At the same time, the corresponding creep strains do not accumulate as rapidly as they should when strain hardening theory is used.

Further comments are in order regarding Figs 7 and 8. It is well known [see Riedel (1981, 1987)] that the asymptotic stresses and strains are of $O\{[1/(n+1)\}$ and $O\{(n/(n+1)\}$, respectively. When Figs 7 and 8 are plotted on a log–log scale, this means that the stresses and strains will plot as straight lines with a slope of $\{1/(n+1)\}$ and $\{n/(n+1)\}$, respectively. These slope values are indeed observed before unloading occurs, i.e. at time less than 24 h. At the end of the unload/reload sequences (times = 49, 74, 99 h), the stresses when a Murakami–Ohno creep law is used are not inconsistent with a slope of $\{1/(n+1)\}$

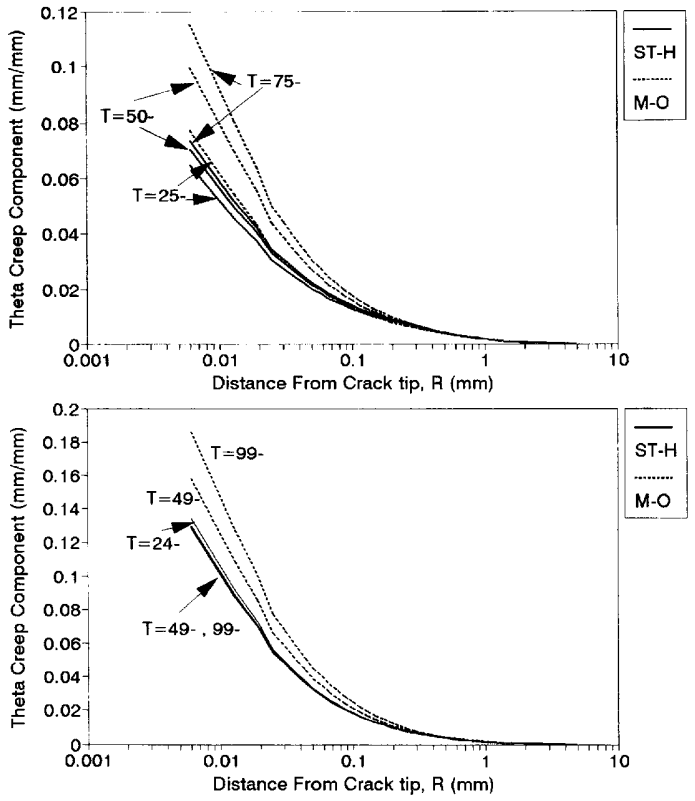

Fig. 8. ε_θ^c Component of total creep strain along $\theta = 0$ line ahead of crack. 9 Cr–Mo steel with $R = 0$. (a) End of unload-hold times. (b) End of reload-hold times.

over a short region. However, the region of dominance of this field is much smaller than the logarithmic singularity. The creep strains of Fig. 8 (with the Murakami–Ohno law), when plotted on a log–log scale, do continue to drift from a slope of $\{n/(n+1)\}$ after each unload/reload cycle, although they are linear over a short range on these plots. For instance, the slope changes from $\{n/(n+1)\} = 0.85$ after a time of 24 h to 0.91 after 99 h (three unload/reload sequences).

The results of this section raise questions regarding the use of the classical approach to creep fracture problems when the cracked structure experiences cyclic loads. The classical approach performs well under constant load conditions. However, under history dependent loading conditions, the asymptotic fields with a strain hardening constitutive law change, perhaps after each load cycle. Classical approaches to creep fatigue life predictions assume that crack growth may be assumed to consist of a fatigue portion and a creep crack growth portion [see, for instance, Jaske (1985)], i.e. Miners rule is used. The contributions of fatigue and creep are assumed to be uncoupled. Since the classical approach to creep crack growth correlates crack growth rates with the strength of the asymptotic fields, and the asymptotic fields change with load cycles, one cannot expect this same rate parameter to perform well under these conditions. In other words, using a parameter which is based on the strength of an asymptotic field may not be adequate when the asymptotic fields continually change. Moreover, since these asymptotic fields are developed by using constitutive laws that are inadequate under cyclic load conditions, one cannot expect the strength of these fields to have meaning outside their range of validity. With these concepts in mind, we proceed by defining and using energy-based parameters in the simulations of creep crack growth experiments, which will be discussed later. Before showing these simulations, these alternative parameters are briefly discussed.

4.3. *Energetic or integral fracture parameters*

Making a choice as to which fracture parameters to focus on when attempting to characterize variable load or history dependent creep crack growth is difficult. We can label the different types of approaches as asymptotic approaches, damage or local approaches, and energetic or integral approaches. Asymptotic approaches are not considered here for reasons summarized above. Local or damage-based approaches, summarized in the recent book by Lemaitre and Chaboche (1990) and the numerous references cited therein, are very useful for predicting crack nucleation for all types of problems, including creep. For crack problems, however, there appears to be a difficulty. The procedure for both coupled and uncoupled damage theories consists of (i) developing the critical material parameter, D_c (scalar or tensor), and (ii) determining a critical length parameter, l_c, i.e. the degree of finite element refinement near the crack tip, so that experimental behavior is predicted. This same critical dimension is required for all other analyses. Because damage localizes at the crack tip, one finds that predicted results become more and more conservative as the mesh becomes more refined. This is because the finer the mesh, the greater are the stress and strain magnitudes and gradients near the crack tip become [see Giovanola and Kirkpatrick (1992) for example]. This type of behavior renders such methods, in the view of this author, to be insufficiently general to extend their use to history dependent creep fracture problems. The approach considered here is based on integral parameters. A general summary of this type of approach has been provided by Kim and van Stone (1992) and for creep problems by Brust and Majumdar (1994). For completeness, a summary of integral approaches is provided here.

Integral parameters. A number of integral parameters have been defined in recent years for application to non-linear fracture mechanics. Blackburn (1972) defined an integral, J_B, the $\hat{J}$-integral was defined by Kishimoto *et al.* (1980), and other integral parameters have been suggested by McClintock (1971), and Watanabe (1985). Cherepanov (1967) first defined the Γ-integral, which was later called ΔT^* and T^* integrals by Atluri (1982), Nishioka and Atluri (1983), Brust *et al.* (1985, 1986), Brust and Atluri ((1986), and Brust and Majumdar (1994) in the context of creep fracture). A review of these integrals has recently been provided by Cherepanov (1989), and a review of a number of other integral parameters has recently been provided by Kim and Orange (1988) and Brust *et al.* (1989) in the context of thermal gradients.

The definition of the integrals in the notation defined below is:
Blackburn (1972):

$$J_B = \int_{\Gamma_1} (\tfrac{1}{2}\sigma_{ij}\varepsilon_{ij}n_1 - t_i u_{i,1})\,d\Gamma; \tag{8}$$

Kishimoto *et al.* (1980):

$$\hat{J} = \int_{\Gamma_1} (W_e n_1 - t_i u_{i,1})\,d\Gamma; \tag{9}$$

Cherepanov (1967), Atluri (1982), Nishioka (1983), Nakagaki (1985), and Brust (1985):

$$T^* = \int_{\Gamma_1} (W n_1 - t_i u_{i,1})\,d\Gamma; \tag{10}$$

McClintock (1971):

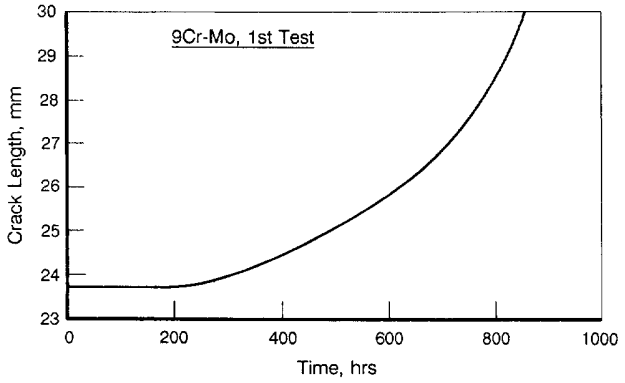

Fig. 9. Crack length versus time behavior for the test in Fig. 4a. The finite element model was forced to follow this crack growth relation.

$$J_M = \int_{\Gamma_\varepsilon} (-t_i u_{i,1})\, d\Gamma; \tag{11}$$

Watanabe (1985):

$$J_W = \int_{\Gamma_\varepsilon} (W n_1)\, d\Gamma. \tag{12}$$

In eqns (8)–(12), the integrals are integrated along a line path defined as Γ_ε. The path shape and other practical considerations are discussed by Brust and Atluri (1986) and Brust and Majumdar (1994), and in many references cited therein. In eqns 8–12, $\boldsymbol{\sigma}$, $\boldsymbol{\varepsilon}$, and $\hat{n}$ are the stress, total strain, and unit normal to the path, respectively, with x_1, and x_2 parallel and normal to the crack growth direction, respectively; t_i is the traction at the path point $(\hat{n} \cdot \boldsymbol{\sigma})$, **u** are displacements, and W is the stress work. The parameter W_e in eqn (9) is the elastic stress work. Note that $T^* = J_M + J_W$ always.

The physical interpretation of the T^*-integral is as an approximation of energy flux to the crack tip region and, as such, depends on the size of the path chosen, i.e. Γ_ε. Detailed discussion regarding the physical significance of the integrals, the path size, and other important considerations is provided by Brust and Majumdar (1994) and Brust *et al.* (1985).

4.4. *Analysis of an experiment*

The experiment discussed above and illustrated in Fig. 4 was modeled in its entirety. The load spectrum of Fig. 4(a) was applied. The experimentally determined crack growth versus time relationship shown in Fig. 9 was also imposed. The finite element mesh utilized is illustrated in Fig. 10. The side groove depth in these specimens was 20% of the thickness. (The nominal thickness was 25.4 mm.) Plane stress solutions were performed, since the creep zones were large here. The loads illustrated in Fig. 4 are the total applied load. The adequacy of this degree of mesh refinement was verified in two ways. First, several constant load cases were analyzed, and the C^*-integral and the C_h^*-integral [respectively, for analyses using the second and first terms of eqn (1) only] were evaluated numerically and compared with handbook solutions. Secondly, two identical analyses were performed by using the extremely refined mesh used to produce the asymptotic solutions for Section 4.2, and the mesh of Fig. 10 over the first 192 h of this test, before crack growth began. The crack initiated 192 h after the test began. All of the integrals discussed above were evaluated on numerous paths for both meshes. The numerical values of the integrals compared within 1% for path sizes greater than 0.3 mm. By observing Fig. 10(b), this means that we can expect numerically accurate results outside a buffer zone of about two elements outside the crack tip.

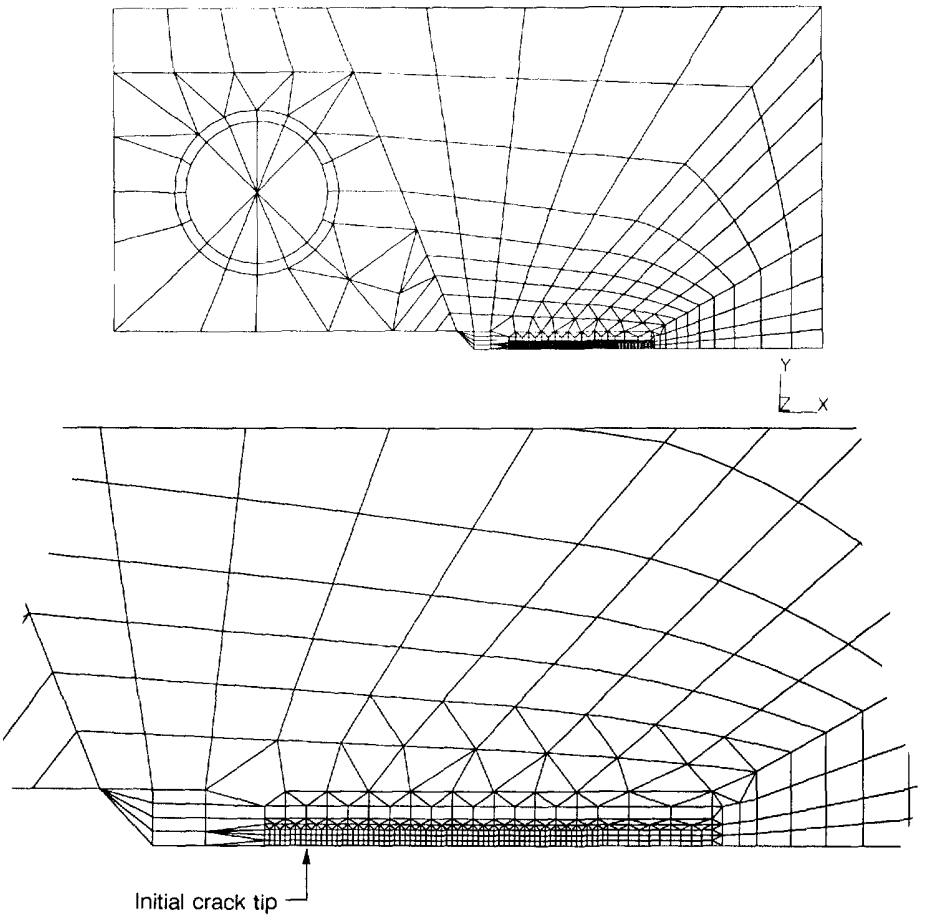

Fig. 10. Finite element mesh used to model test. (a) Overall mesh. (b) Mesh blow-up near the crack tip. The elements near the crack tip are 0.15-mm-square elements.

The material properties were those listed in Section 4.2 for the 9 Cr–Mo steel at 538° C. The two other constants needed to utilize eqn (1) are:

$$A_1 = 1.362 \times 10^{-50}, \quad n_1 = 18.86$$

for stress in Mpa and time in hours.

Figure 11(a) shows the compressive stress immediately after unloading at $t = 343$ h, i.e. before stress relaxation occurs. The finite element grid is shown so that the reader can obtain a feel for the size scales involved. Recall that the elements near the crack tip are square with a side length of 0.15 mm. The contour levels shown in these figures represent the magnitudes at the *outside edge* of the shading (the large stress gradients should be clear). Figure 11(b) shows the stresses after creep relaxation has occurred after the 0.1-h unload-hold period. Note the significant size of the compressive zone. Comparing compressive residual stress zone sizes at later times and comparing these with Fig. 11, one observes that the magnitudes of the compressive stresses after relaxation are continually increasing as the crack size increases, as expected.

Figure 12 shows the size of the compressive $\sigma_{\gamma\gamma}$ zone behind the wake of the growing crack at a time of 628 h. This is at a time when the full load is on the specimen, and the crack has just completed growing through an element. Such a compressive wake zone is known to exist for elastic–plastic growing cracks [see, for instance, Rice *et al.* (1980)], and here it is shown to occur for growing creep cracks. The known asymptotic solutions for growing cracks using simple constitutive laws also exhibit this compressive wake zone feature [(see Riedel (1987), for instance)] for plane stress, but not for plane strain. The

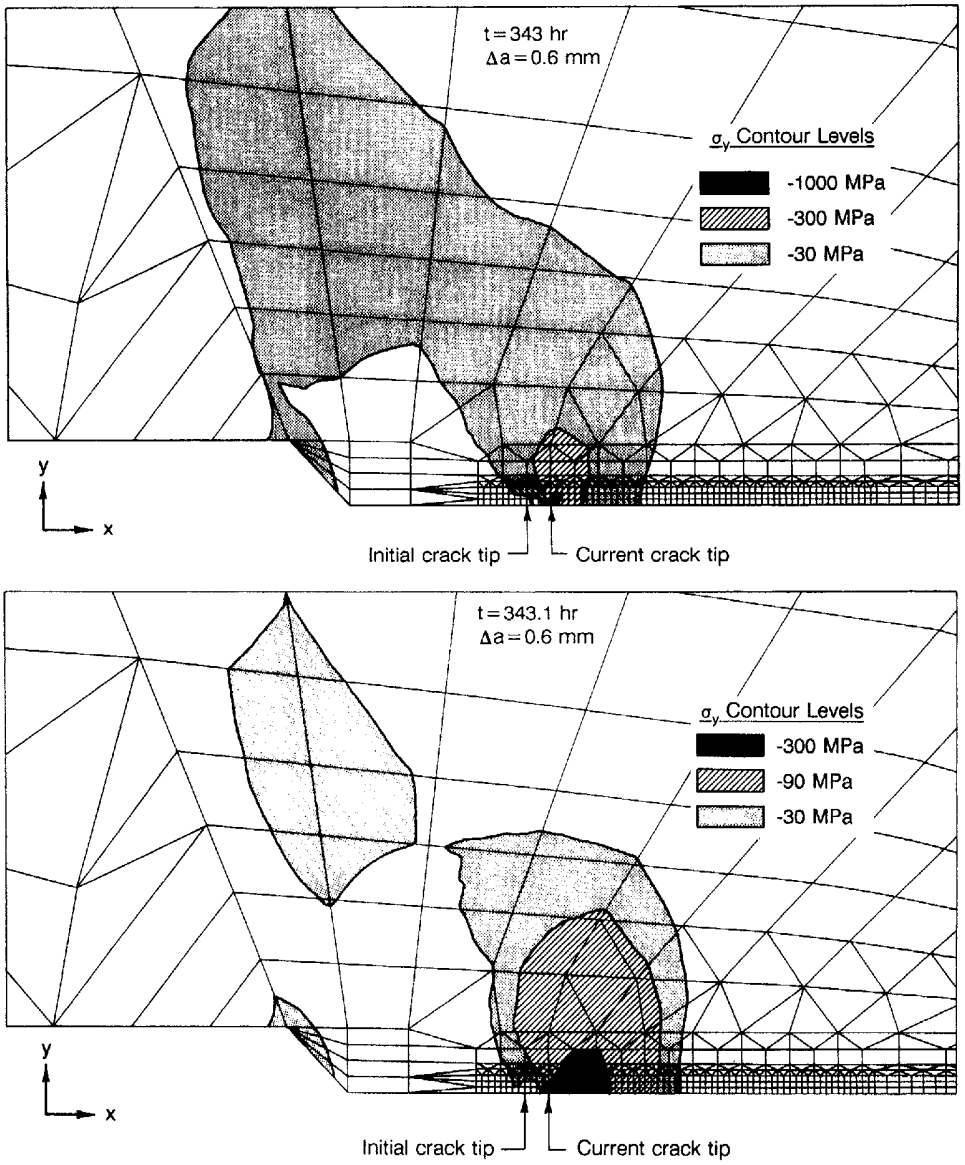

Fig. 11. Contour plots of σ_y near the time of 343 h. The contour levels represent the values at the outermost border of the shade. The size of the elements along the crack growth direction near the tip is 0.15 mm along the side. (a) Stresses just after unloading, before stress relaxation occurs. (b) Stress after the 0.1-h unload-hold period of relaxation has occurred.

compressive zone size seen here is much larger than that predicted from asymptotic solutions. The stresses in this zone are not insignificant, with a maximum stress in the compressive wake shown in Fig. 12 of -300 Mpa.

Displacement comparisons. The experimental and analytically predicted displacements are compared over the first 192 h of the test, before crack growth begins, in Fig. 13. The extremely refined mesh used in Section 4.2 was used for these predictions. The experimental results are slightly higher than the predicted values. Note that, for the analysis, the crack was assumed to begin growing at a time of 192 h after the beginning of the test. However, as indicated in Fig. 13, small amounts of crack growth actually occurred before this time, which, in part, accounts for the underprediction of the analysis. An analysis assuming a constant load is also plotted here, showing that there is a continual drift upward of

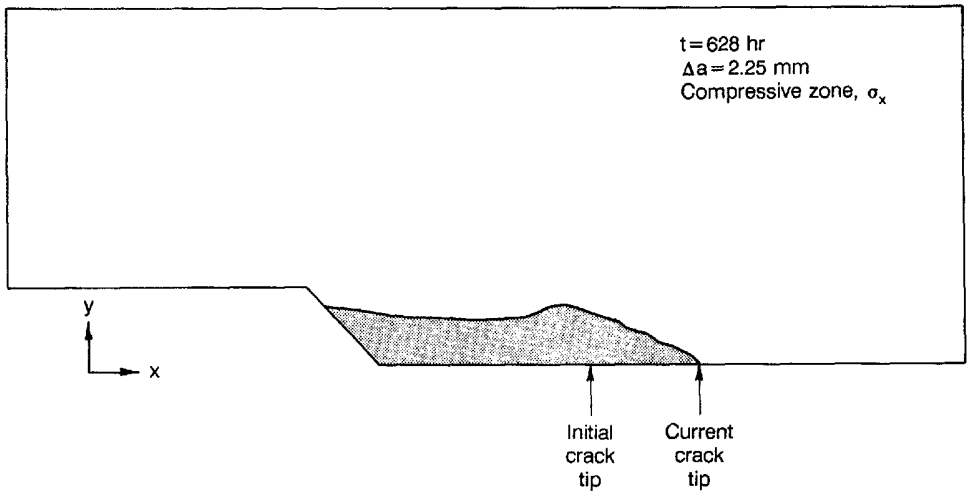

Fig. 12. Compressive wake zone for the growing creep crack. The maximum stress is −300 MPa in this region.

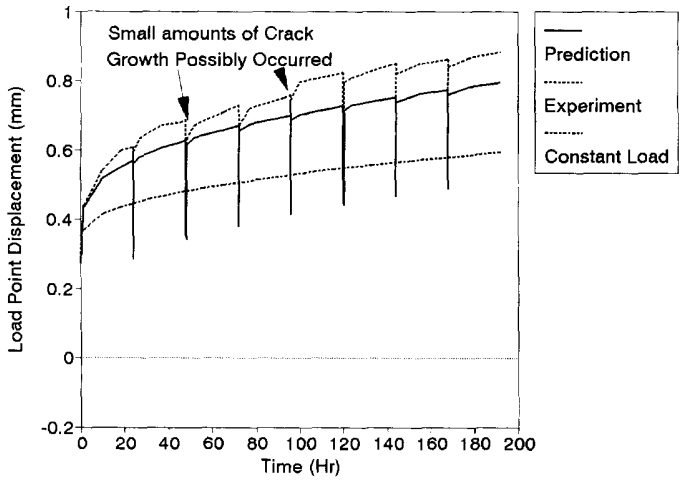

Fig. 13. Comparison between experimental and predicted load point displacements for the 9 Cr–Mo test before crack growth. The lower curve represents results for the constant load case.

the variable load solution owing to the increased strain rates that develop after each cycle.

Figures 14(a)–14(c) show some of the details of the displacement comparisons over shorter time periods. Figure 14(a) shows what happened very early in the test. The precise load history shown in Fig. 4 was not strictly followed in this particular test. There were a few times during the test where the load was held longer than 24 h before unloading. (It will be clear in some of the later figures when this occurred.) At the beginning of the test, some differences also occurred. A load of 19.94 kN was first applied to the specimen and held for 0.05 h. The specimen was then unloaded and held for 0.033 h before loading to 23.353 kN and following the general sequence of Fig. 4. (This was done to provide a check on the experimental set-up.) This means that the first unloading actually occurred about 5 min after the start of the test. Figure 14(a) details the displacements over the first 2 h of the test. Note the effect of the first unload cycle on the displacement predictions. It is also clear here that the displacement rates due to the first cycle of load increase significantly compared with having no cycle. Figure 14(b) details the displacements between 110 and 180 h after the test began. Note that the displacement rates after an unload cycle are greater than those before the unloading. This effect becomes more important after crack growth

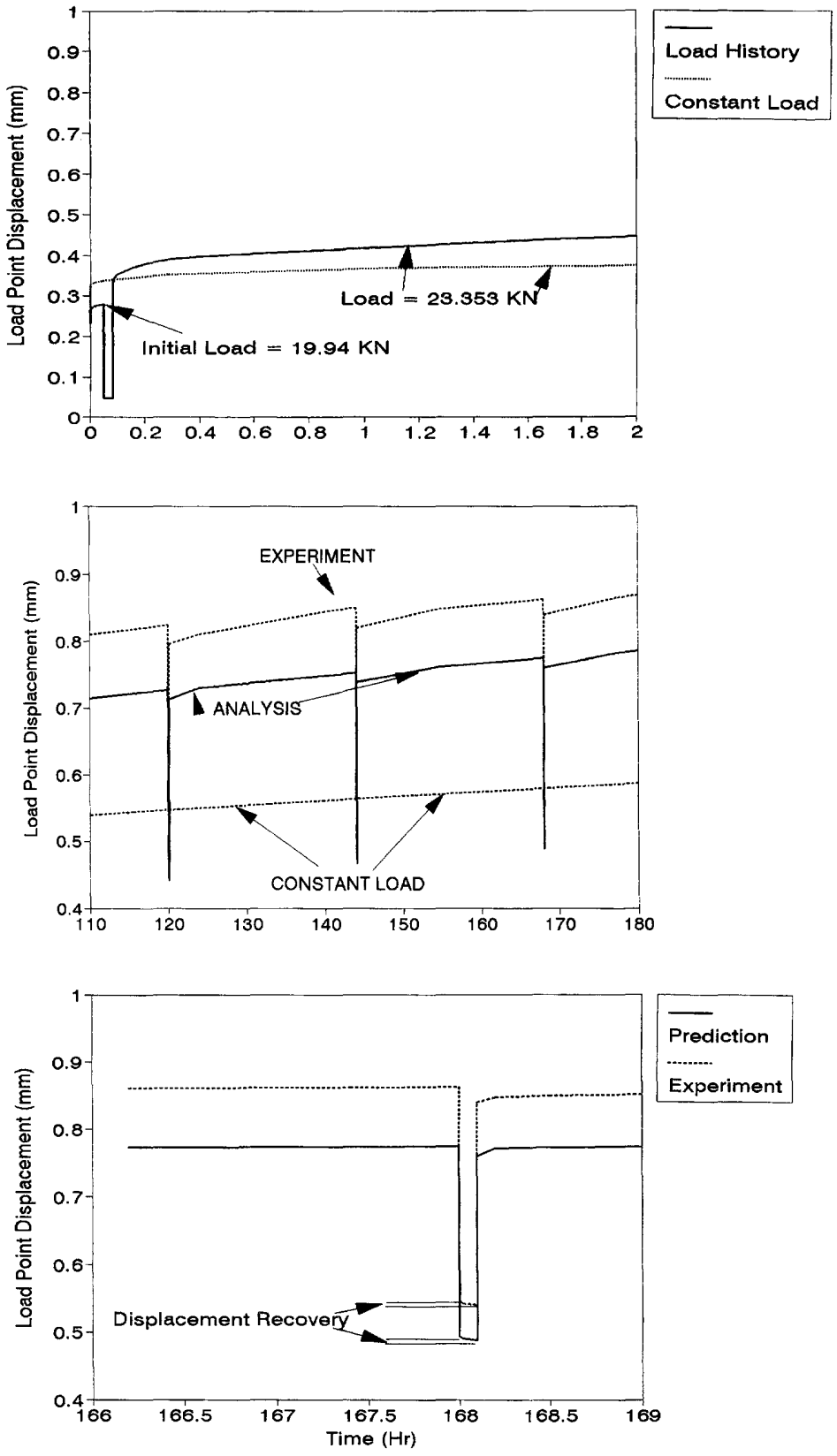

Fig. 14. Details of displacement versus time comparisons at specific times before crack growth begins. (a) Comparison of predicted results for variable load and constant load cases. (b) Detailed comparison of three unload cycles between 110 and 180 h. (c) Comparison of displacements during the load at time of 168 h.

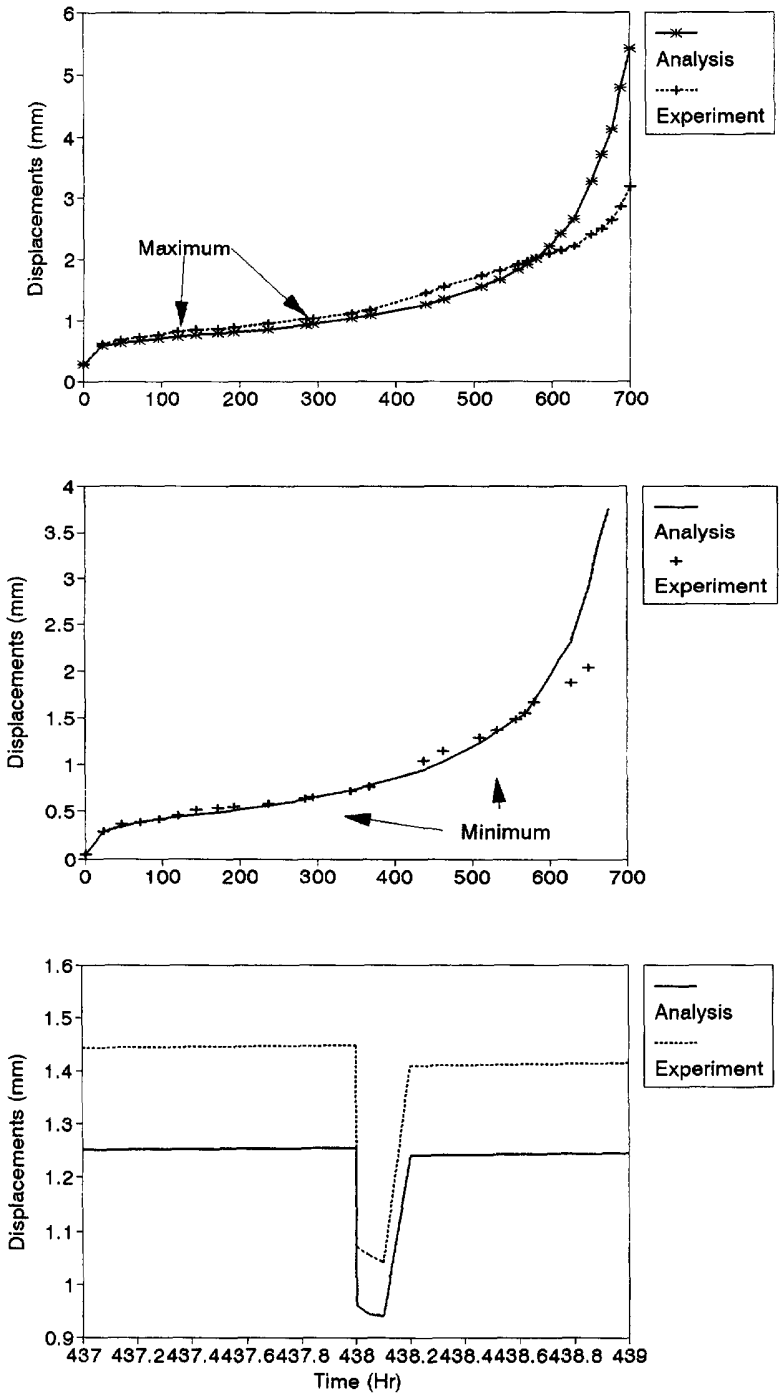

Fig. 15. Comparison of displacements for 9 Cr–Mo test. (a) Maximum displacements at the end of the reload-hold times. (b) Minimum displacements at the end of the unload-hold times. (c) Displacement comparison for the unload–reload cycle at time = 438 h.

commences, as will be shown shortly, and was discussed relative to Figs 2 and 4. Figure 14(c) shows displacement recovery at a time of 168 h.

Figure 15 shows the predicted and experimentally determined displacements over the entire test. Figure 15(a) shows the maximum displacements, i.e. at the end of reload and hold periods, throughout the entire test. The experimental and predicted displacements compare quite well until about 600 h. After this time, the predicted displacements overpredict the experimental values. This overprediction after 600 h essentially means that

failure was predicted a little earlier analytically than the experimental results showed. The experiment showed that the displacements began to rise sharply at about 650 h, prior to failure at about 710 h. This difference between the analysis and experiment may be due, in part, to the use of a plane stress assumption for the analysis. Figure 15(b) provides a comparison of the minimum displacements, i.e. at the end of the unload-hold periods. Again the comparison is quite reasonable. Figure 15(c) shows a detail of predicted and experimental displacements during the unload that occurred in the 438th hour of the test. Here the displacement recovery and the reduced displacement compared with the values before unloading, and the increased displacement rates due to the cycle are evident. Note from Fig. 15(a) that this comparison at a time of 438 h is made for the time when the difference between prediction and analysis is nearly the maximum for times less than 600 h. The results of Fig. 15 give us confidence that the numerical model compares reasonably with experimental data. The predictions provided next for the integral parameters are therefore likewise considered to be reasonably accurate.

Integral parameters. The behavior of the integral parameters is somewhat different before and after crack growth. Let us first look at the behavior for a constant load case with no crack growth before providing the predictions of the integrals for this particular test. Consider loading the compact tension specimen to 23.353 kN and holding it for 2000 h. The integral parameters should be path independent in the region of dominance of the asymptotic fields if the fields are separable and if terms like $\sigma \cdot \varepsilon$ are of $O(1/r)$ [see Willis (1975) and Moran and Shih (1987)]. Figure 16(a) shows the behavior of the T^*-integral evaluated on four paths of radius $R = 0.3$, 0.45, 0.6, and 0.8 mm. These paths are circular in shape and traverse the stationary crack tip. (The refined focused mesh used for the asymptotic studies was used for this constant load case only.) This figure suggests that the integrals are independent of path. In fact, all the integral parameters behave this way, including J_W and J_M, even though these two integrals are not path-independent even for the elastic problem. This suggests that the region of dominance of the asymptotic fields is quite large. This observation of a large zone of dominance for the asymptotic field was also made in Section 4.2, which examined the asymptotic fields themselves. Indeed, this is an alternative technique to determine the region of dominance of the asymptotic fields. Observing Figs 16(b) and 16(c), however, note that both T^* and J_W are not path-independent. Figure 16(b) is actually a blow-up of Fig. 16(a) over the first 10 h. The initial load is applied elastically, this being followed by the relaxation of the elastic singularity via creep deformation. Apparently, the conditions for path independence discussed above are violated for a very short period of time (less than about 0.05 h). One can see that the integrals are path-dependent for early times, and then the same difference between the paths is maintained over the rest of the analysis. Since:

$$T^* = \int_0^t \dot{T}^* \, \mathrm{d}t \tag{13}$$

throughout the entire load history, it is clear that the integral rates are path-dependent for a short period after application of the load, after which the rates of the integrals become path-independent. This effect was checked by using several different mesh refinements, and several different degrees of time step refinement, and appears to be real.

Now we return to the analysis of the experiment of Fig. 4 and discuss the behavior of these integral parameters during cyclic loading. Figure 17a shows the behavior of the J_W-integral for the variable load case, also evaluated along four different-sized circular paths emanating from the stationary crack tip. These plots show the first 192 h of the test analysis results, before crack growth commences. Several interesting observations can be made. (i) After each change in load path, a step function increase in the integral occurs. (Note here that the first unload actually occurred after only 0.05 h of testing; hence, large differences between the paths are observed early.) Such a step function change suggests that the unloads induce increased damage to the crack tip region. (ii) The value of the integral is larger as

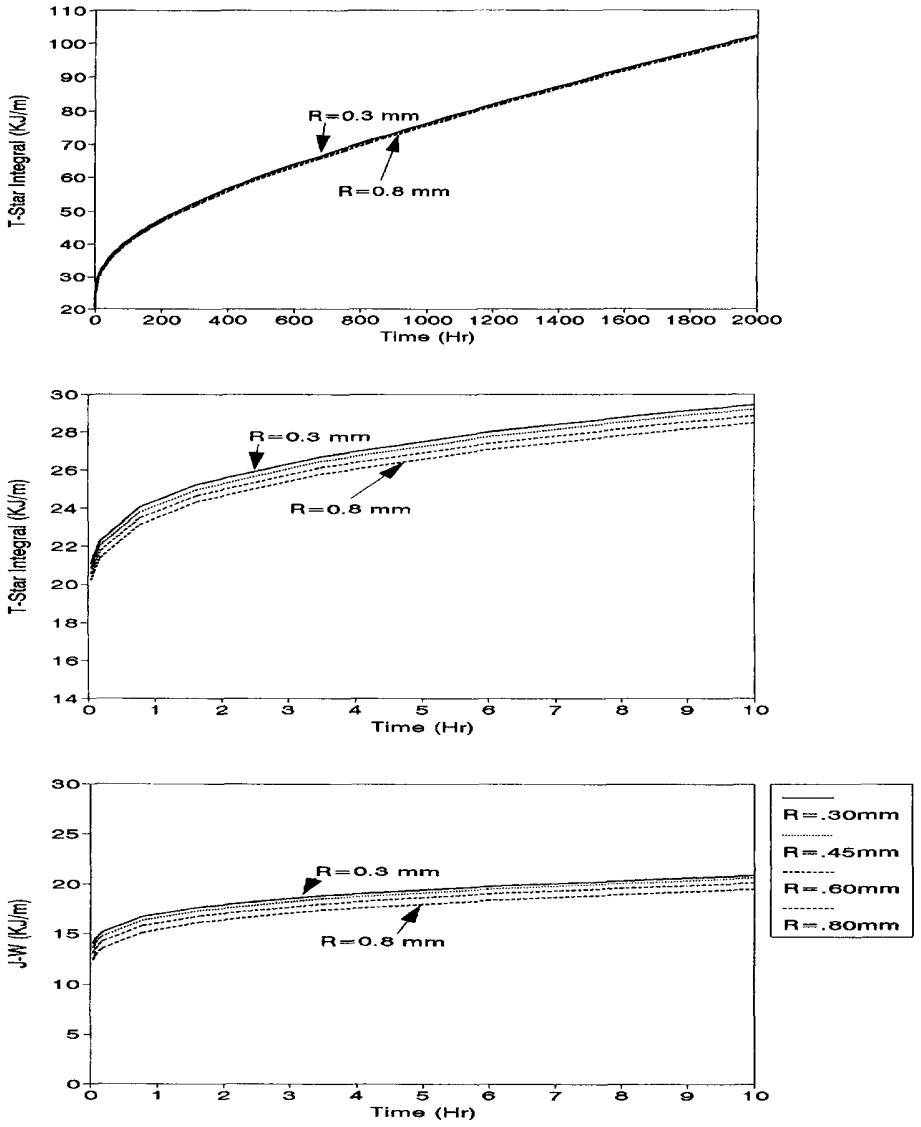

Fig. 16. Behavior of the integral parameters evaluated along different-sized circular paths (R = 0.3, 0.45, 0.60, and 0.80 mm) for the constant load case. (a) T^*-integral over the entire time period. (b) T^*-integral from 0 to 10 h. (c) J_w-integral from 0 to 10 h.

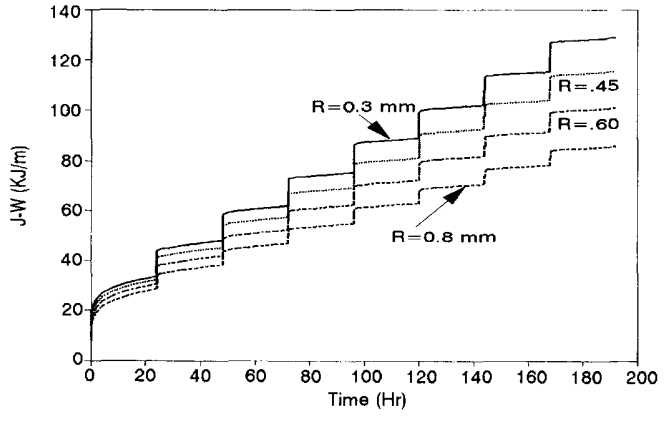

Fig. 17a. J_w-integral plotted as a function for the variable load test before crack growth begins; R is the radius of the circular path emanating from the crack tip.

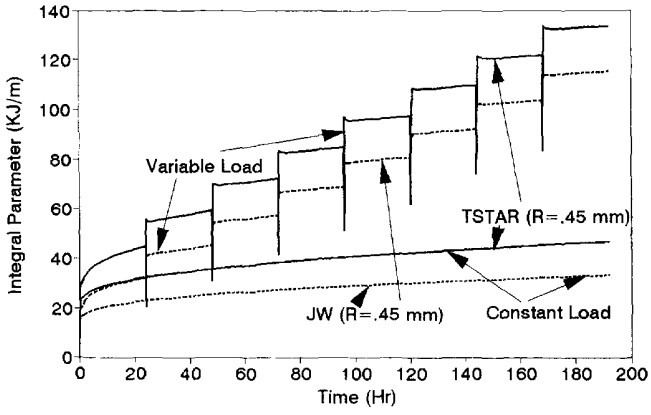

Fig. 17b. T^*- and J_w-integrals. Comparison between the constant load and variable load cases. The path size, R, is 0.45 mm.

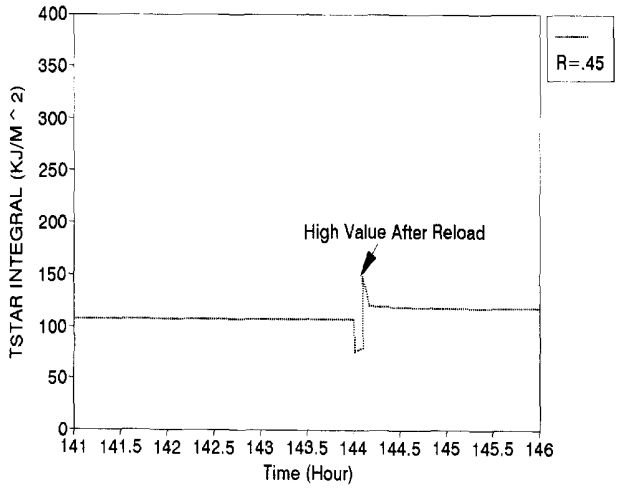

Fig. 17c. Behavior of T^*-integral for unloading at t = 144 h. Crack growth has not begun as yet.

the size of the path *becomes smaller*. In addition, it is clear that the integral is becoming more and more path-dependent, further suggesting that the asymptotic fields change, perhaps with each cycle, and further violate the conditions for path-independence in the region of asymptotic fields (i.e. separable fields, etc.). It should also be mentioned that the rates of J_W are also path-dependent even near the end of each of the reload-hold (24-h) periods. Clearly, these results, coupled with those presented in Section 4.2, suggest that the classical approach to creep fracture, i.e. the search for the strength of an asymptotic field, may not be practical under variable load conditions since the crack tip fields change significantly as unloads take place. *The trends illustrated in Fig. 17a occur for all five integrals considered here.*

Figure 17b shows the T^*- and J_W-integrals for a path radius of 0.45 mm for both the variable load and the constant load cases. Note that the T^*-integral decreases during an unload (see also Fig. 17c), whereas J_w does not. The constant load values of the integrals are also shown in Fig.17b. The effect of the unloads is to increase the crack tip severity if these integrals are crack tip characterization parameters. Finally, the behavior of the T^*-integral after an unload/reload sequence can be observed in Fig. 17c. Figure 17c shows an enlargement of the unload performance of the T^*-integral at a time of 144 h. Immediately after reloading, the integral attains a large value, which reduces very rapidly over short times to a steadily increasing value. All integrals behave in this way for the stationary crack problem. For the growing crack, this effect is not seen. It is believed that this is an artifact of the Murakami–Ohno constitutive law used. The plots of the integrals as a function of

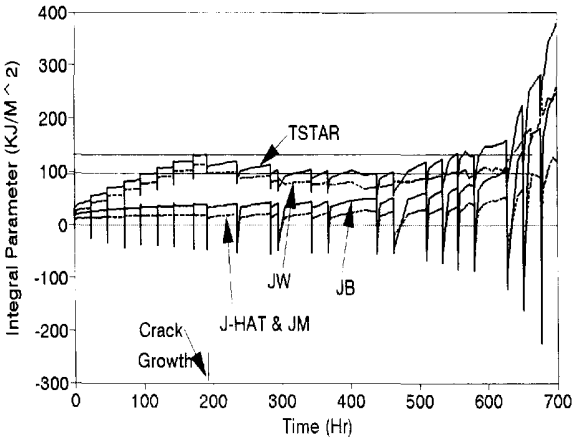

Fig. 18. Integral parameters plotted against time for complete analysis of test.

time do not include these large spikes, which occur over very short times after reloading. Rather, the first integral value plotted is typically after about 0.1 h after the reload-hold time begins to eliminate this artifact.

Figure 18 compares all the integral parameters as a function of time. This is for a value of the path size equal to 0.45 mm. Brust and Majumdar (1994) discuss the practical evaluation of these parameters in detail for the growing crack problem. The T^*- and J_W-integrals both experience a step jump after each cycle, as discussed earlier, before crack growth begins. The J_B-, $\hat{J}$-, and J_M-integrals also do so, but to a much smaller extent. Note that the J_M and $\hat{J}$ parameters are almost identical. This is because the W_e term in $\hat{J}$, which is the elastic stress work, is very small, as it is for nearly all non-linear problems [see eqn (9)]. Also observe that the experimental scheme of Fig. 4 is not strictly adhered to, since several times 48 h elapsed, and once 72 h, before an unload cycle. Further note that the T^*-integral attains a nearly constant value (close to the nucleation value) throughout the entire time history (between 100 and 130 kJ/m^2, as indicated by the lines in Fig. 18). This suggests that a constant value of T^* may characterize crack growth under creep fatigue conditions. The same comment applies to J_W.

The T^*- and J_W-integrals are plotted as a function of the path size in Figs 19a and 19b, respectively. These figures show the values of the integrals at the end of the hold periods only. It may be seen that, before crack growth occurs, the paths closest to the crack tip maintain larger magnitudes than the larger paths. After crack growth, however, a trend in the opposite direction begins, with the larger paths giving slightly larger values. The larger values after crack growth are expected because of the interpretation (discussed in Section 4.3) of the integrals as an energy loss per unit crack extension, to a finite-sized region (i.e. the value of the path size R) in the vicinity of the growing crack tip. The larger R is, the greater is the energy that may be deposited into the crack tip region. Values for the path size of $R = 0.3$ mm, which is probably too close to the crack tip, and subject to numerical errors, were not plotted here. The values of the integrals, especially after crack growth begins, are nearly independent of the path size. This is a very important result because it suggests that we may choose any value of R for our definition of the resistance curve, as long as R is small enough to capture the energy losses due to the crack only. For practical application of these parameters, the largest value of R that is feasible is desired in order to minimize computational costs.

It is also important to comment that the values of these integrals are independent of the finite element grid size chosen. For instance, if the same analysis is performed by using a grid twice as refined as the mesh used here, and the integrals are calculated on the same size of paths as those used here (i.e. $R = 0.45$, 0.6, etc.), the same resistance curve is obtained. This was shown here for the stationary crack portion of the analysis by using the meshes of Section 4.2 and Fig. 10 and was demonstrated by Brust *et al.* (1985), using four different meshes for the elastic–plastic crack growth problem.

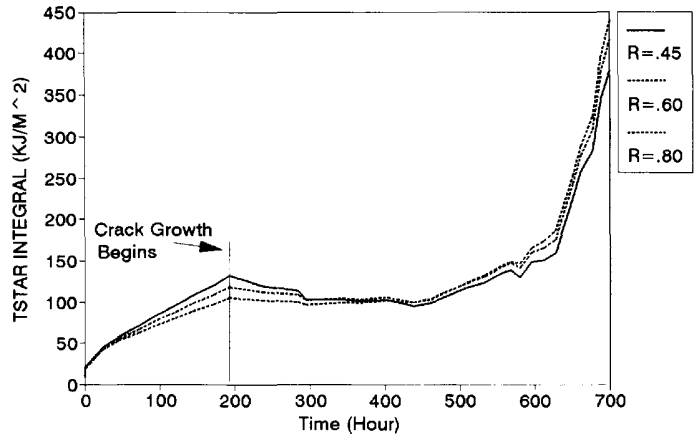

Fig. 19a. T^*-integral versus time for several definitions of path size, R.

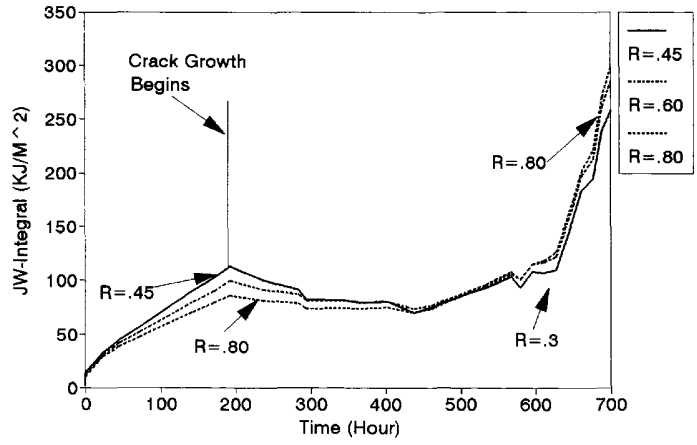

Fig. 19b. J_w-integral versus time for several definitions of path size, R.

The resistance curves are plotted in Figs 20a–20c for $R = 0.45$ and 0.8 mm. Note the nearly constant value that the T^*- and J_W-integral resistance curves maintain during crack growth. The J_M-integral, on the other hand (Fig. 20c), continually increases during crack growth at a nearly constant rate (especially for $R = 0.8$ mm). After about 628 h, the curves become unstable, suggesting that unstable creep failure is predicted. The predicted

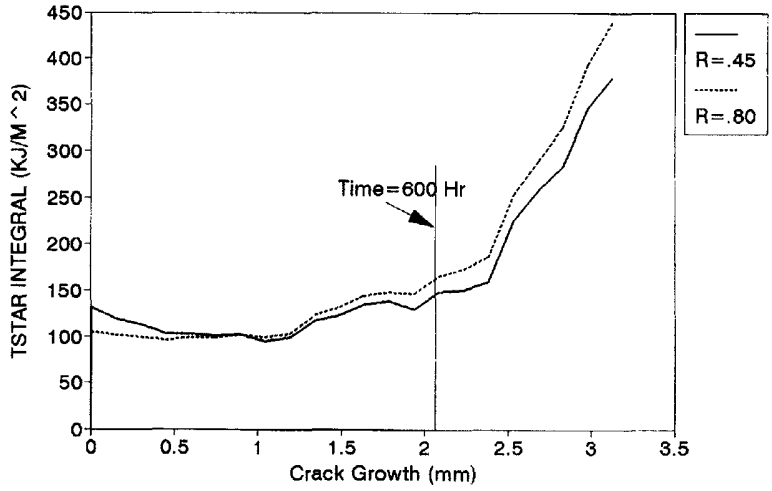

Fig. 20a. T^*-resistance curves. Instability begins after about 600 h.

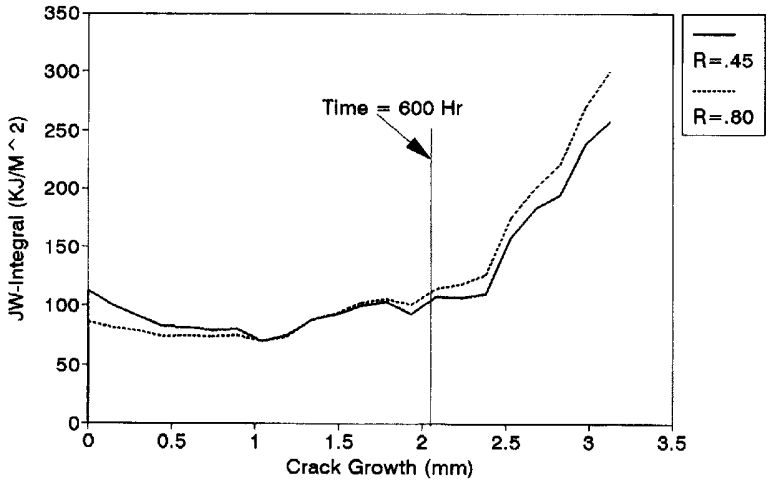

Fig. 20b. J_w-resistance curve.

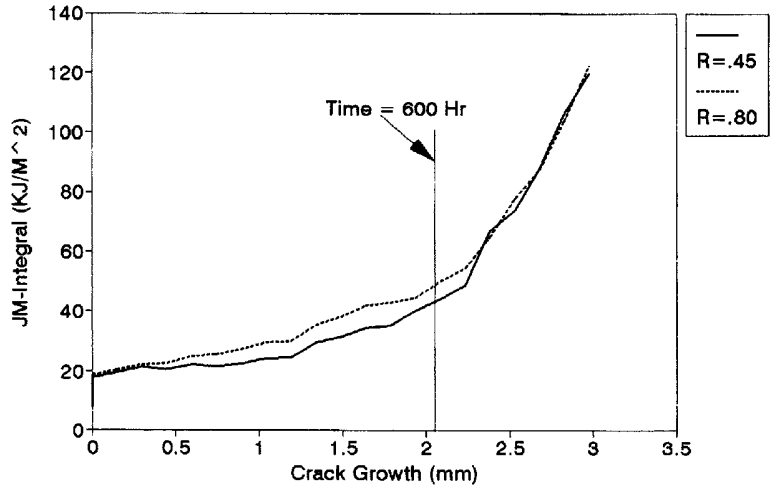

Fig. 20c. J_M-resistance curve.

instability point for this analysis compares reasonably well with the experimental results, especially considering the two-dimensional nature of the analysis.

The nearly constant saturation values for T^* and J_W during crack growth suggest that these parameters may be used as a creep fracture parameter for cyclic creep. The fact that they are not perfectly uniform is due to three-dimensional crack-growth effects and the plane-stress assumption. Moreover, errors in crack growth measurements can certainly affect results. However, this suggests that these integrals may be used to predict crack initiation as well as growth by using the value at initiation throughout the history. In addition, creep crack nucleation and reinitiation may also be predicted. The J_M-integral may likewise be used, with its resistance curve continually increasing. However, because the T^*-integral has a physical interpretation, it may be the most useful of the parameters. Crack nucleation or crack reinitiation during history dependent loading would be predicted by using this constant value of the resistance curve of Fig. 20a.

5. CONCLUSIONS

The subject of creep-crack growth behavior under variable load conditions was investigated here. The importance of large creep strain rates which develop after stress reversals was shown to have a strong influence on the deformation response of a cracked creep

specimen. Classical creep-crack approaches for variable load creep-fatigue conditions were critically examined. It was determined that such approaches, which are based on obtaining the strength of asymptotic crack tip fields, may not be sufficiently general because the fields appear to break down and change as the number of load cycles increases. The possibility of using alternative integral fracture parameters for characterizing the variable load creep-crack growth process was examined. While certainly not conclusive, the potential for using these alternative parameters for characterizing this complex process of crack behavior appears promising. Further work is necessary, is ongoing, and will be reported in the near future.

Acknowledgements—This work was supported by the U.S. Department of Energy, Office of Basic Engineering Sciences, under Grant No. DE-FG02-90ER14135. The author thanks Dr O. Manley and S. Datta for their support. The author would also like to thank Dr Bhaskar Majumdar for directing the experimental efforts.

REFERENCES

Atluri, S. N. (1982). Path independent integrals in finite elasticity and inelasticity, with body forces, inertia, and arbitrary crack-face conditions. *Engng Fract. Mech.* **16,** 341–364.

Bassani, J. L. and McClintock, F. A. (1981). Creep relaxation of stress around a crack tip. *Int. J. Solids Structures* **17,** 479–492.

Blackburn, W. S. (1972). Path independent integrals to predict onset of crack instability in an elastic plastic material. *Int. J. Fract.* **8,** 343–346.

Brust, F. W. and Atluri, S. N. (1986). Studies on creep crack growth using the T^*-integral. *Engng Fract. Mech.* **23,** 551–574.

Brust, F. W. and Leis, B. N. (1992). A new model for characterizing primary creep damage. *Int. J. Fract.* **54,** 45–63.

Brust, F. W. and Majumdar, B. S. (1994). Load history effects on creep-crack growth. *Engng Fract. Mech.*

Brust, F. W., Nishioka, T., Atluri, S. N. and Nakagaki, M. (1985). Further studies on elastic–plastic stable fracture utilizing T^*-integral. *Engng Fract. Mech.* **22,** 1079–1103.

Brust, F. W., McGowan, J. J. and Atluri, S. N. (1986). A combined numerical/experimental study of ductile crack growth after a large unloading using T^*, J, and CTOA criteria. *Engng Fract. Mech.* **23,** 537–550.

Brust, F. W., Nakagaki, M. and Springfield, C. W. (1989). Integral parameters for thermal fracture. *Engng Fract. Mech.* **33,** 561–579.

Brust, F. W., Krishnaswamy, P. and Majumdar, B. S. (1993). Further studies of history-dependent loading in the creep-crack growth regime. In *Fracture Mechanics—Applications and New Materials* (PVP-Vol. 260), pp. 49–58. American Society of Mechanical Engineers, New York, NY, USA.

Cherepanov, G. P. (1967). Crack propagation in continuous media. *Appl. Math. Mech.* **31,** 467–488.

Cherepanov, G. P. (1989). A remark on the dynamic invariant or path-independent integral. *Int. J. Solids Structures* **25,** 1267–1269.

Gittus, J. (1975). *Viscoelasticity and Creep Fracture in Solids*. Applied Science, London.

Giovanola, J. H. and Kirkpatrick, S. W. (1992). Advances in Fracture/Damage Models for the Analysis of Engineering Problems (ASME Publication AD-Vol. 137), pp. 285–303.

Goldman, N. L., and Hutchinson, J. W. (1975). Fully-plastic crack problems: the center cracked strip under plane strain. *Int. J. Solids Structures* **11,** 575–592.

Inoue, T. *et al.* (1991). Evaluation of inelastic constitutive models under plasticity-creep interaction condition. *Nucl. Engng Des.* **126,** 1–11.

Jaske, C. E. (1984). Topical report on damage accumulation by crack growth under creep and fatigue, Ph.D. thesis, Ohio State University, USA (also Department of Energy Report for Contract No. W-7405-ENG-92-131).

Kim, K. S. and Orange, T. W. (1988). A review of path-independent integrals in elastic–plastic fracture mechanics. In *Fracture Mechanics: Eighteenth Symposium* (ASTM STP 945), American Society for Testing and Materials, Philadelphia, PA, USA, pp. 713–729.

Kim, K. S. and van Stone, R. H. (1992). Elevated temperature crack growth, NASA Final Report, NASA CR-189191.

Kishimoto, K., Aoki, S. and Sakata, M. (1980). On the path independent integral. *J. Engng Fract. Mech.* **13,** 841–850.

Krishnaswamy, P., Brust, F. W. and Ghadiali, N. D. (1993). Finite element analysis of history dependent damage in time dependent fracture mechanics. *ASME J. Press. Vessel Technol.* **115,** 339–347.

Krishnaswamy, P., Brust, F. W. and Ghadiali, N. D. (1994). A finite element algorithm to study creep crack growth based on the creep hardening surface. *Int. J. Num. Meth. Engng*, in print.

Lemaitre, J., and Chaboche, J. L. (1990). *Mechanics of Solid Materials*. Cambridge University Press, Cambridge, UK.

Leung, C. P., McDowell, D. L. and Saxena, A. (1988). Influence of primary creep in the estimation of C_t parameter. *Int. J. Fract.* **36,** 275–289.

McClintock, F. A. (1971) in *Fracture* 3 (Edited by H. Liebowitz), Academic Press.

Moran, B. and Shih, C. F. (1987). Crack tip and associated domain integrals from momentum and energy balance, *Engng Fract. Mech.* **27,** 615–62.

Murakami, S. and Ohno, N. (1982). A constitutive equation of creep based on the concept of a creep hardening surface. *Int. J. Solids Structures* **18, 67,** 597–609.

Nicholas, T. and Weerasooriya, T. (1985). A model for creep fatigue interactions in alloy 718 (ASTM STP 868), pp. 167–180. American Society for Testing and Materials, Philadelphia, PA, USA.

Nicholas, T. and Weerasooriya, T., (1986). Hold-time effects in elevated temperature fatigue crack propagation (ASTM STP 905), pp. 167–180. American Society for Testing and Materials, Philadelphia, PA, USA.

Nishioka, T. and Atluri, S. N. (1983). Path independent integrals, energy release rates, and general solutions of near-tip fields in mixed-mode dynamic fracture mechanics, *Engng Fract. Mech.* **18,** 1–22.

Ohno, N., Murakami, S. and Ueno, T. (1985). A constitutive model of creep describing creep recovery and material softening caused by stress reversals. *J. Engng Mater. Technol.* **107,** pp. 1–6.

Rice, J. R., Drugan, W. J. and Sham, T. L. (1980). Elastic–plastic analysis of growing cracks (ASTM STP 700) pp. 189–221. American Society for Testing and Materials, Philadelphia, PA, USA.

Riedel, H. (1981). Creep deformation at crack tips in elastic–viscoplastic solids. *J. Mech. Phys. Solids* **29,** 35–49.

Riedel, H. (1987). *Fracture at High Temperatures.* Springer-Verlag, Berlin, Germany.

Riedel, H. and Rice, J. R. (1980). Tensile cracks in creeping solids. In *Fracture Mechanics: Twelfth Conference* (ASTM STP 700), pp. 112–130. American Society for Testing and Materials, Philadelphia, PA, USA.

Saxena, A. and Han, J. (1986). Evaluation of crack tip parameters for characterizing crack growth behavior in creeping materials. ASTM Task Group Report E24.08.071E.24.04.08.

Saxena, A. (1991). Creep crack growth in high temperature ductile materials. *Engng Fract. Mech.* **40,** 721–736.

Shih, C. F. and German, M. D. (1981). Requirements for a one parameter characterization of crack tip fields by the HRR singularity. *Int. J. Fract.* **17,** 27–43.

Watanabe, K. (1985). The conservation law related to path independent integral and expression of crack energy density by path independent integral, *Bull. Japan Soc. Mech. Engrs* **28,** 26–33.

Willis, J. R. (1975). Equations of motion for propagating cracks. In *The Mechanics and Physics of Fracture*, pp. 57–67. The Metal Society.

Yokabori, T. and Yokobori, A. T., Jr (1984). Some notes to the high temperature crack growth rates and probabilistic fracture mechanics approach, respectively. In *Proceedings of ICF6*, New Delhi, India, 4–10 December, pp. 273–294.